Diffraction Anomalous Fine Structure :

A new technique for probing local atomic environment

Ingrid J. Pickering[1], Michael Sansone[2], James Marsch[2] and Graham N. George[1]

1. *Stanford Linear Accelarator Center, Stanford Synchrotron Radiation Laboratory,*

Stanford University, Stanford, CA 94309, USA

2. *Exxon Research and Engineering Company, Route 22 East,*

Annandale, NJ 08801

Abstract: Diffraction anomalous fine structure (DAFS) is the fine structure in the intensity of an X-ray diffraction peak in the vicinity of an absorption edge. DAFS is measured by monitoring the intensity of a diffraction peak as a function of the incident X-ray energy as it is scanned through an absorption edge. It combines the short range structural sensitivity of X-ray absorption spectroscopy with the long range periodicity of X-ray diffraction, and can provide structural information which is not available from these techniques alone, or in combination. We demonstrate the technique for several different dilute, polycrystalline samples, and present an iterative data analysis method which allows the extraction of a specific X-ray absorbance spectrum from the DAFS spectrum. We demonstrate the ability of DAFS to distinguish between the local environments in each component of a physical mixture of two phases, and to separate the contributions to the X-ray absorption spectrum of the tetrahedral and octahedral cobalt sites in the spinel Co_3O_4. Finally, we have used DAFS to study the polarized X-ray absorption spectra from polycrystalline $K_2Ni(CN)_4$.

Introduction

X-ray diffraction and X-ray absorption fine structure (XAFS) spectroscopy are both well-established techniques for structural investigations of samples in the solid state. The XAFS can be divided into two components, the absorption edge-spectrum, also referred to as near-edge X-ray absorption fine structure (NEXAFS), or X-ray absorption near-edge fine structure (XANES), and the extended X-ray absorption fine structure (EXAFS). The edge spectra result from X-ray induced transitions of the core-electron (e.g. a 1s electron for a K-edge) to unoccupied levels, and are thus very sensitive to electronic structure. The EXAFS results from scattering of an ejected core-electron by neighboring atoms, and is used to probe the local structure within a material. X-ray diffraction results from the coherent scattering of X-rays by an array of atoms with longer range order. When the X-ray energy, E, is near an absorption edge of a constituent atom, then the atomic scattering factor for X-rays, f, is comprised of a Thompson scattering term, f_0, plus an energy-dependent "anomalous" contribution; $f = f_0 + f'(E) + if''(E)$. The energy tunability of synchrotron radiation sources affords a convenient method of selectively changing the scattering from component atoms, and this has been exploited in numerous crystallographic studies for crystal structure phasing e.g. the multiple wavelength anomalous dispersion (MAD) technique for phasing protein crystal structures [1]. The imaginary part of the anomalous scattering factor $f''(E)$ is simply proportional to the product of the X-ray absorption cross-section and the X-ray energy, and $f''(E)$ and $f'(E)$ are interrelated by their mutual Kramers-Kronig dispersion integrals (see below). It follows that the anomalous scattering is expected to contain structure analogous to the EXAFS and edge spectra, and this has been observed experimentally in numerous studies [cf. 2,3]. X-ray absorption edges are highly sensitive to oxidation state and electronic environment with corresponding changes in the X-ray anomalous scattering. This has been used to study the valence distributions in several mixed-valence materials e.g. Eu_3O_4 [4], $GaCl_2$ [5], $YBa_2Cu_3O_{6+\delta}$ [6], and $Y_3Fe_5O_{12}$ and $Y_3Ga_5O_{12}$ [7] (note that anomalous diffraction is also called resonant X-ray diffraction [3,6b]).

In the present work we investigate the detailed energy dependence of the fine structure of the anomalous diffraction for a number of powder materials. There have been numerous early observations of such fine structure [e.g. 2,3,6,7,8], and the same physical phenomenon has been given a variety of different appellations, including DIFFRAXAFS (diffraction-XAFS; by Pickering et al. 9]), and BREFS (Bragg reflectivity extended fine structure, by Arcon et al. [3]).

In an attempt to establish a common nomenclature, we have now adopted the nomenclature of Stragier *et al.*, who have suggested DAFS (diffraction anomalous fine structure) [10]. Arcon *et al.* observed DAFS from a single crystal of copper sulfate, and showed that it contains structure which is phase-shifted by 90° with respect to the EXAFS (*ie.* cosine instead of sine terms in the EXAFS equation) [3]. Attfield has used DAFS of the (001) and (111) Bragg peaks to obtain site resolved Cu K-edge X-ray absorption spectra of the high temperature superconductor $YBa_2Cu_3O_{6.27}$, although at rather limited energy resolution with only 14 data points in each spectrum [7b]. Very recently, in an elegant study, Stragier *et al.* [10] have reported a quantitative theory, together with the DAFS of copper metal using the (111) and (222) reflections of a 2000Å thick Cu(111) epitaxial film. Their theory confirms and extends the finding of Arcon *et al.* [3] that the DAFS is comprised of a sum of sine and cosine contributions, corresponding to the fine structure of the $f''(E)$ and $f'(E)$ components, respectively. Stragier *et al.* [10] have also developed procedures for quantitative analysis of the DAFS oscillations, although a fore-knowledge of the crystal structure is required in order to determine the relative contributions of $f''(E)$ and $f'(E)$ to the fine structure. Additionally, a direct comparison of DAFS edge spectra with X-ray absorption edge spectra becomes quite problematic. The DAFS in the edge region generally has a negative cusp shaped structure, with edge structure present as derivative-like features, contrasting with the absorption spectrum, which has peaks corresponding to transitions to bound states, and a step at the threshold energy.

There are several areas in which DAFS has important potential applications, and these include *(i)* the separation of the XAFS from mixtures of crystalline compounds of unknown structure, *(ii)* site specific XAFS spectra from a single phase with more than one type of a given atom, and *(iii)* obtaining polarized XAFS from powder samples. The goal of the present work is to assess the utility of DAFS as a structural tool. To this end we have performed DAFS studies of dilute powder samples for each of the three application areas outlined above (it is important to note that powder DAFS is experimentally somewhat more difficult than single crystal DAFS, due to the much lower count rates in the powder case). We present an analysis method which allows extraction of XAFS from the DAFS which does not depend upon a detailed knowledge of the crystal structure. Finally, we will discuss potential applications of DAFS in structural chemistry, materials science, and in biophysics.

Experimental

Sample Preparation. Unless otherwise stated, all materials were obtained from the Aldrich Chemical Co. at the highest purity available, and were used without further purification. Typical sample preparation involved grinding in an agate ball mill for 20 minutes, followed by further grinding with a diluent compound for approximately 5 minutes. Around 100-200 mg of the resulting mixture was then pressed under approximately 10 tons pressure into a 20 mm-diameter disk, with a final thickness of about 0.4 mm. Ideal candidates for the diluent material combine a low X-ray absorption coefficient with good pressing characteristics. Various solids were tested, and two, the polymer polyvinylpolypyrrolidone (PVPP, Sigma) and lithium carbonate, were used in the experiments described in this paper. Li_2CO_3 forms somewhat fragile disks, and although its sharp diffraction peaks can be used as a control for analysis methods (see below), these may overlap a peak of interest. Away from its diffraction peaks, Li_2CO_3 has a very low scattered background. PVPP forms very robust disks of excellent quality, and has no sharp diffraction peaks, but does have a scattered background level which tends to add noise to measurements of the lowest intensity peaks. A sample of $K_2Ni(CN)_4$ was synthesized according to published procedures [11].

Data collection. DAFS data collection was carried out on beamline X10C at the National Synchrotron Light Source [12,13]. Either Si(111) or Si(220) double crystal monochromators were used, together with a downstream focusing mirror positioned to reject higher order reflections from the monochromator. Figure 1 shows a schematic diagram of the equipment, which involves elements of both powder X-ray diffraction and XAFS experiments. The relevant experimental components in the path of the X-ray beam were as follows. Collimating slits set at 5mm were used to horizontally define the X-ray beam, followed by a beam position monitor and vertical collimating slits set at *ca.* 0.5 mm. The beam position monitor (a position sensitive ion chamber) was coupled via a feed-back loop to a piezoelectric transducer controlling the tilt angle of an upstream focusing mirror [14] so as to remove small X-ray beam movements, and maintain a constant position of the beam entering the experiment. This was followed by an evacuated flight path, and then a further set of horizontal and vertical collimating slits to reject scattered radiation. An incident beam (I_0) monitor (either a sodium iodide scintillation detector or an ion chamber) was placed immediately following the scatter slits. Samples were mounted

on a flat aluminum plate having a central hole to allow passage of the transmitted X-ray beam, and were aligned at the center of the θ circle of a 2-circle diffractometer. A 12" nitrogen-filled ion chamber was placed after the sample to detect the beam intensity transmitted by the sample (I_1) as in a conventional transmittance XAFS experiment. Linearities of the I_0 and I_1 detectors were measured by scanning the X-ray energy over the range of interest, before insertion of the sample, and appropriate corrections applied so as to obtain the true sample absorbance. An energy dispersive SiLi detector (EG&G Ortec) was mounted on the 2θ arm of the diffractometer to measure the scattered intensity I_d, and the fluorescent intensity I_f. The light incident on this detector was apertured by two sets of slits (see Figure 1), typically set at 0.5mm vertical and 6mm horizontal. The distance from the sample to the SiLi detector was about 39cm. The output of the SiLi detector was fed via a Gaussian shaping amplifier to single channel analyzers which were used to select counts of photons in the desired energy range. The linearity of the energy dispersive detector was checked by scanning the offset of one of the monochromator crystals so as to provide a variation in incident beam intensity, and the detector was found in all cases to be operating in the pseudo-linear regime, with insignificant losses due to electronic dead times.

Data collection was carried out on a Digital Equipment Corporation micro-VAX II computer using specially developed software. Data reduction and analysis were carried out either on the beamline computer, a VAX 8350 computer at Exxon Research and Engineering, or on VAXstation 4000 computers at SSRL. Figure 2A illustrates the data collection procedure for a 5wt.% sample of $KMnO_4$ in lithium carbonate. At each energy point a small θ-2θ scan was carried out to collect the diffraction peak profile, with the midpoint of the scan defined by the X-ray energy and the *d*-spacing of the Bragg peak of interest. The X-ray energy was incremented as for a typical XAFS scan, with the θ-2θ diffractometer position tracking the peak centroid. In general, sufficient data points were collected to obtain a diffraction peak profile (*ca.* 15-21 points, see Figure 2A). The voltage range of single channel analyzer used to monitor the elastic scatter signal from the energy dispersive detector was controlled by the computer so as to follow the motions of the monochromator (and thus the energy of the elastically scattered radiation) during data collection. Good detector energy resolution was found to be important in order to reject the bulk of the X-ray fluorescence, and an amplifier shaping time of 2 μsec was used. The integrated intensity of the diffraction peak was obtained by fitting each individual θ-2θ scan with a pseudo-Voigt peak-shape, together with a low order polynomial to remove back-

ground signal. The latter was predominantly K_β fluorescence admitted to the single channel analyzer elastic scatter window due to the energy resolution of the detector.

Angular and absorption corrections of diffracted intensity. The scattered intensity I_d, normalized by the incident beam intensity I_0, must first be corrected for the bulk absorption effects, which are distinct from the DAFS oscillations [9]. The absorbance A of a sample of perpendicular thickness t at angle θ is given by $A=\log(I_0/I_1)=\mu t/\sin\theta$ where μ is the bulk absorption coefficient. The absorption attenuation of a diffracted beam due to a thin plate of sample in the $\theta-2\theta$ geometry is simply proportional to $D=(1-e^{-2A})/A\sin\theta$, where A is the absorbance of the plate simultaneously measured as described above [9]. It was found experimentally that optimum signal to noise was obtained when the sample absorbance at energies just above the X-ray absorption edge was of the order of unity. Thus, the optimum sample path length for transmittance XAS [*cf.* 15] is also optimal for DAFS.

The intensity of the diffracted beam will also be affected by the Lorentz factor, $L=2\sin^2\theta\cos\theta$; the beam is close to 100% plane polarized in the horizontal plane and therefore, with upward reflecting geometry, no polarization correction is required. Thus the diffracted intensity can be converted to obtain a quantity proportional to the square of the structure factor by multiplying by L/D. Figure 2B shows the uncorrected DAFS spectrum, together with the Lorentz-absorbance corrected DAFS spectrum (subsequently referred to as the "raw" DAFS spectrum) and the absorbance for the 5 wt.% $KMnO_4$ sample of Figure 2A.

Theory and data analysis

DAFS theory. When an X-ray photon interacts with an atom, one of several things can happen; the photon can be elastically scattered (Thompson scattering), or it can be inelastically scattered (*e.g.* Compton scattering, Raman scattering). If the energy of the incident X-ray is in the vicinity of an absorption edge, then the photon can additionally be absorbed, or can undergo other inelastic scattering processes such as resonant Raman X-ray scattering [16]. In this work we are concerned only with the coherent elastic scattering, which is known as Bragg scattering. As mentioned above, the energy dependent part of the coherent elastic scattering is given by the so-called anomalous correction.

The DAFS spectrum includes contributions from both $f'(E)$ and $f''(E)$ in varying

proportions depending upon both the crystal structure, and the specific diffraction peak measured. There are therefore difficulties in a detailed interpretation of spectral features without further analysis. In order to conveniently obtain quantitative information from the spectrum, we have developed computer software to extract the pure $f'(E)$ contribution from the DAFS spectrum which can be converted into an $f''(E)$ function, and thence into a site-specific absorbance. The method requires no *a priori* knowledge of the crystal structure, and therefore can be applied to a wide variety of problems.

The intensity of a diffraction peak is proportional to $|F|^2$ where F is the structure factor of the diffraction peak, which is given, assuming site occupancies to be unity, by:

$$F = \sum_r f_r \exp\left(2\pi i \phi_r\right) = \sum_r f_r \cos\left(2\pi \phi_r\right) + i \sum_r f_r \sin\left(2\pi \phi_r\right) \qquad (1)$$

where ϕ_r is the phase factor [17] of an individual atom for the specific diffraction peak, f_r is the atomic scattering factor for atom r, and the summation is over all atoms in the unit cell. If we neglect temperature factors for brevity [18], the atomic scattering factor can be expressed as:

$$f(E) = f_0 + f'(E) + if''(E) \qquad (2)$$

where $f'(E)$ and $f''(E)$ are the real and imaginary contributions to the anomalous scattering of the atom, which becomes significant in the vicinity of an absorption edge of the atom. The imaginary part of the anomalous scattering factor, $f''(E)$, is proportional to the X-ray absorption cross section $\sigma(E)$ multiplied by the photon energy, E, and $f'(E)$ and $f''(E)$ are related by their mutual Kramers-Kronig relationships:

$$f''(E) = \left(\frac{mcE}{2e^2h}\right) \sigma(E) \qquad (3)$$

$$f'(E_0) = \frac{2}{\pi} \int_0^\infty \frac{E f''(E)}{(E_0^2 - E^2)} dE \qquad (4)$$

$$f''(E_0) = -\frac{2E_0}{\pi} \int_0^\infty \frac{f'(E)}{(E_0^2 - E^2)} \, dE \tag{5}$$

Here, m is the rest mass of the electron and c, e and h have their usual meanings. It can be shown that the diffracted peak intensity is simply proportional to:

$$|F|^2 = \left(A^2 + B^2\right) + 2\left(A\alpha + B\beta\right)f_m'(E) + 2\left(B\alpha - A\beta\right)f_m''(E)$$
$$+ \left(\alpha^2 + \beta^2\right)\left\{\left[f_m'(E)\right]^2 + \left[f_m''(E)\right]^2\right\} \tag{6}$$

with:
$$A = \sum_r f_{0,r} \cos(2\pi\phi_r) \qquad \alpha = \sum_m \cos(2\pi\phi_m)$$

$$B = \sum_r f_{0,r} \sin(2\pi\phi_r) \qquad \beta = \sum_m \sin(2\pi\phi_m)$$

where m is the sum over all anomalous atoms in the unit cell. A and B are the real and imaginary components of the structure factor in the absence of anomalous effects and are energy-independent. α and β, also energy-independent, are simply the sums of the sine and cosines of the phases of the anomalous atoms, respectively [19].

In the case of a centrosymmetric unit cell, sine terms cancel throughout and B and β are zero. Equation 6 therefore reduces to an equation with only two coefficients:

$$|F|^2 = A^2 + 2\alpha A f_m'(E) + \alpha^2\left(f_m'(E)^2 + f_m''(E)^2\right) \tag{7}$$

Equation 7 is general for several distinct anomalous atoms in a centrosymmetric cell. In this general case, $f_m'(E) = \frac{1}{\alpha}\sum_i \alpha_i f_i'(E)$ and $f_m''(E) = \frac{1}{\alpha}\sum_i \alpha_i f_i''(E)$, where $\alpha = \sum_i \alpha_i$ and the sum is over each distinct type of anomalous atom. Thus for more than one type of anomalous atom contributing, the final $f_m''(E)$ (and hence absorbance) is a mean value weighted according to the phases of the constituent atoms. This weighting varies between diffraction peaks, and also is different from the weighting of components for the bulk absorbance, and therefore a combination of observations may be used to deconvolute the contributions from different at-

oms. In the case that there is only one crystallographically distinct atom contributing to a particular Bragg peak, then the final $f_m''(E)$ is for that atom alone and the final absorbance extracted is for that single component.

A set of predictive computer programs were written, based on the theory described above, and using theoretical [20] or XAFS-derived model compound values for $f'(E)$ and $f''(E)$. These allow prediction of the size of the DAFS, and the contribution from discrete sites, for any known structure, and hence assist in the choice of the diffraction peak for study. The predicted effects agreed excellently with the experimental measurements (below), confirming that the programs were performing accurately. The size of the predicted DAFS varies considerably from reflection to reflection, and both cusp-shaped (positive peak) or, more commonly, inverted cusp-shaped curves can occur. Often small, seemingly insignificant, diffraction peaks have very large DAFS, making them the best candidates for study.

Extraction of XAFS from the DAFS spectrum. In all the systems studied in this paper, centrosymmetric unit cells have been used, and we will now restrict our discussions to this case. Equation 7 is solved iteratively to obtain the functions $f_m'(E)$ and $f_m''(E)$, in the following way. Initial estimates for $f_m'(E)$ and $f_m''(E)$ are obtained from Cromer-Liberman theory [20], and are used to estimate the ratio α/A plus a linear scaling function by fitting equation 7 to the ends of the data, excluding the highly structured region near the absorption edge, using non-linear regression techniques. Note that the absolute values of A and α are not obtained by this method. Equation 7 is then solved for the function $f_m'(E)$, from which $f_m''(E)$ is readily obtained by Kramers-Kronig transformation. These new estimates for $f_m'(E)$ and $f_m''(E)$ are then used to obtain new estimates for A and α, and the procedure repeated until the residual between calculated (from Equation 7) and experimental curves approaches a minimum. The function $f_m''(E)$ can easily be converted into absorption coefficient using Equation 3. The cycle described above can also be carried out by solving for $f_m''(E)$ and transforming to obtain a new $f_m'(E)$. The XAFS spectrum obtained using this method can then be analyzed using all the familiar tools and programs that are available for XAFS analysis. The results of this procedure are illustrated in Figure 3 for the $KMnO_4$ sample of Figure 2. Figure 3A shows the $f'(E)$ and $f''(E)$ functions as extracted using the iterative procedure, and Figure 3B the corresponding DAFS-extracted XAFS, together with the XAFS. A value for the ratio α/A of 0.04 was estimated from the extraction procedure for the $KMnO_4$ (211) DAFS, which agrees well with the value of 0.03

estimated from the crystal structure. The excellent correspondence of the two spectra in Figure 3B demonstrate that the procedure is working correctly. This method can readily be extended to non-centrosymmetric structures by using a greater number of refinable coefficients (see 19).

It should be noted that the effectiveness of this procedure pivots upon having a fast and accurate procedure for performing Kramers-Kronig integrals. We adopted the method of Templeton and Templeton [21] in which the smooth theoretical curve [20] (appropriately convoluted with a broadening function) for $f''(E)$ (or $f'(E)$) is subtracted from the data to obtain a fine structure function $\delta f''(E)$. $\delta f''(E)$ tends to zero outside the range of the data and therefore the integral in Equation 4 (and 5) needs only to be evaluated over the limits of the data. For most calculations we used a fast Fourier transform method [22] to evaluate the Kramers-Kronig integral (Equations 4, 5) (note that an accurate scale factor is important for this method to be effective). The resulting scattering factor fine structure $\delta f'(E)$ can then be combined with the theory $f'(E)$ to calculate the total value. In earlier analyses, we extrapolated the experimental data with theory to span a total range from 10eV to 200,000eV, and evaluated the Kramers-Kronig integral over this range. No significant difference, other than speed of computation, between the two methods was found. The later routine was tested by repeatedly transforming a test data set (calculated from an XAFS spectrum of $KMnO_4$) between f'' and f', and comparing the end result with the original. Only a marginal broadening of sharp spectral features was observed after fifty cycles of Kramers-Kronig transforms.

Polarization in DAFS. The plane-polarized nature of a synchrotron X-ray beam is now frequently exploited in XAFS to probe directionality within a single crystal. Typically, the angle between the X-ray electric field vector, or e-vector, and a unique molecular direction within the crystal is varied, and the responses of various spectral features are determined. Although powders which have been oriented by dint of a preferred crystallite morphology or other phenomenon may also yield directional information through XAFS, a randomly oriented powder cannot, by definition, give directional information in XAFS, since the crystallites have a random spatial distribution with respect to the e-vector. However, in a random powder sample diffracting an incident, plane-polarized X-ray beam, those crystallites which are in the correct orientation for diffraction do have a spatial relationship with the e-vector of the incident beam. In the case of upward-reflecting geometry the e-vector is always normal to the plane containing the incident X-ray beam, the diffracted beam and the normal to the *hkl* plane, *i.e.* the e-vector

will always lie within the *hkl* plane of the Bragg reflection. For a given reflection, contributions to the DAFS will therefore be an average of all possible orientations of the e-vector within the *hkl* plane, but with no contribution from orientations of the e-vector away from the plane. For the dipole-allowed transitions which contribute the major features of X-ray absorption K-edge spectra, the transition intensity I_{if} is proportional to the square of the dipole matrix element $I_{if} \propto |<\psi_f| e \cdot r |\psi_i>|^2 \propto \cos^2\Theta |<\psi_f| r |\psi_i>|^2$, where Θ is the angle between the e-vector and the transition dipole vector r (*e.g.* the the axis of a *p*-orbital for a *1s→np* transition) . Expressed relative to the powder intensity, the transition intensity is simply given by $3\cos^2\Theta$ (the average of $3\cos^2\Theta$ over a sphere is unity). Similarly, for K-edge EXAFS in the plane wave approximation, the orientation dependence of backscattering amplitude is also given by $3\cos^2\Theta$, and in this case Θ is the angle between the e-vector and the absorber-backscatterer (*a-b*) vector. In both cases the powder averaged amplitude is unity. For polarized DAFS of K-edge spectra it is simple to show that the amplitude is proportional to $(3\sin^2\zeta)/2$, where ζ is the angle between the transition dipole vector (or *a-b* vector) and the normal to the *hkl* plane. Thus, the maximum enhancement of a transition relative to the powder case is $^3/_2$ and occurs with the transition vector in the *hkl* plane, *ie.* $\zeta=90°$, and likewise the maximum suppression is zero when $\zeta=0°$. If there is more than one transition vector orientation in a unit cell, or when the multiplicity of the powder diffraction peak is greater than unity (see Results section, below), then the total orientation dependence will simply be the average of the dependencies for the individual vectors. An example of the former would be for differently oriented molecules within the unit cell.

EXAFS analysis. The EXAFS oscillations $\chi(k)$ were analyzed using the approximate equation:

$$\chi(k) \simeq \sum_{i=1}^{n} \frac{N_i A_i(k,R_i)}{kR^2} \exp\left(\frac{-2R_i}{\lambda(k,R_i)}\right) \exp\left(-2\sigma_i^2 k_i^2\right) \sin\left[2kR_i + \Phi(k, R_i)\right] \quad (8)$$

Here, k is the photoelectron wave number, R_i, σ^2_i and N_i are the absorber-backscatterer distance, mean square deviation in R_i (note that this is distinct from the absorption cross-section $\sigma(E)$) and coordination number for atom *i*, respectively. $A_i(k, R_i)$, $\Phi(k, R_i)$ and $\lambda(k, R_i)$ are the curved-wave total amplitude, total phase-shift, and photoelectron mean free path, respectively. The latter were calculated using the program *feff* of Rehr and co-workers [23].

Results

In our preliminary DAFS experiments we set out to determine the feasibility of performing DAFS on dilute powder samples. The difficulty of these experiments is compounded by the fact that the diffracted intensity from a powder sample is very much less than for a single crystal. We will first describe the results of experiments designed to test the ability of the technique to separate XAFS of mixtures and of sites, and then proceed to describe a polarized powder DAFS study of the compound $K_2Ni(CN)_4$.

Separation of Absorption edges of mixtures. It is a common problem in structural science to have a physical mixture of polycrystalline phases of unknown, or only partially known identity. In this case, DAFS can be used in a simple manner to obtain edge and EXAFS spectra of the different phases, whereas XAFS yields only the average of contributions from all the phases. In principle, any diffraction peak from a phase can give information concerning the local structure of a constituent atom, given that there are no special extinctions for the atom of interest. Using our method of deconvolution, it is not necessary to know the crystal structure to be able to extract the contribution from a particular phase; it is sufficient to simply assign the peaks to a specific phase. A similar method can also be applied to separating contributions from a mixture of crystalline and amorphous phases. In this case, the sharp Bragg peaks of the crystalline phase will yield the DAFS from that component, with the broad amorphous component being removed by background subtraction.

In order to test the ability of DAFS to separate the fine structure due to anomalous components from two different phases, we examined a dilute mixture of chromium (III) oxide (2 wt.%) and sodium chromate (2 wt.%) in PVPP. Two adjacent but well-resolved peaks were chosen for the measurements: the (031) Bragg peak of Na_2CrO_4 (d = 2.733Å) and the (104) peak of Cr_2O_3 (d = 2.666Å), and were recorded simultaneously. The resulting DAFS-extracted XAFS spectra of the two components of the mixture are shown in Figure 4, together with the bulk XAFS of the mixture. The dotted lines show the XAFS spectra of the individual components recorded separately. The Cr_2O_3 DAFS spectrum from the mixture shows excellent correspondence with the XAFS of the pure component. The features of the edge, including the weakly quadrupole-allowed *1s→3d* transition at about 5992 eV, are very well reproduced. The signal to noise of this spectrum is good, and excellent separation of this component from the

mixture has been achieved. The intensity of the (031) Bragg peak of Na_2CrO_4 is approximately 50% of that of the (104) peak of Cr_2O_3, and also shows a smaller anomalous effect, and therefore somewhat poorer statistics are obtained for the Na_2CrO_4 (031) DAFS. Additionally, a small amount of contamination of the (031) Na_2CrO_4 signal with that from the neighboring Cr_2O_3 (104) peak may be suggested by the peak at around 6010eV, which corresponds to the strongest feature of the Cr_2O_3 spectrum. Although noisier, it is evident that the XAFS extracted from the DAFS spectrum reproduces the edge spectrum well, and in particular, the $1s \rightarrow 3d$ transition at 5992.8 eV, which gains dipole-allowed intensity from mixing with oxygen p-orbitals [24], is well reproduced both in form and in intensity.

Separation of spectra from two distinct anomalous atoms in one phase.
The oxide Co_3O_4 has the normal spinel structure, in which a cubic close-packed array of oxygens incorporates formally low-spin Co(III) cations at octahedral interstices, and formally high-spin Co(II) cations at tetrahedral interstices. The structure thus contains one tetrahedral cobalt for every two octahedral cobalt sites. Co_3O_4 crystallizes in the cubic space group $Fd\bar{3}m$ No. 227 [25]. From refinement of powder diffraction data we find a value for the unit cell $a_0 =$ 8.0851(2)Å, which agrees well with literature values [26]. The two different cobalt sites occur on high symmetry positions within the unit cell, yielding extra conditions for reflection above the basic spacegroup conditions (i.e. h,k,l either all odd or all even). The tetrahedral cobalt sites (8b) have the additional conditions ($h=2n+1$ or $h,k,l=4n+2$ or $h,k,l=4n$) and the octahedral cobalt sites (16c) the conditions ($h=2n+1$ or $h+k+l=4n$). Hence, there is a small subset of peaks for which only the octahedral cobalt contributes, and another for which only the tetrahedral cobalt contributes. We selected the (222) diffraction peak ($d = 2.334$Å) to study the pure octahedral component, and the (422) diffraction peak ($d = 1.650$Å) for the tetrahedral component. The Co_3O_4 (222) diffraction peak exhibits a particularly large anomalous effect, which is illustrated in Figure 5. The peak has almost zero intensity at 7720 eV, which is close to the absorption edge.

Figure 6 shows the raw DAFS spectra for Co_3O_4 (422) and (222) diffraction peaks, together with the raw cobalt K-edge DAFS spectrum for the ($\bar{1}12$) peak of Li_2CO_3. The Li_2CO_3 spectrum was collected as a control for the absorption correction and intensity extraction procedures and, as expected, shows no structure over the cobalt absorption edge. The

DAFS-extracted site specific cobalt K-edge X-ray absorption spectra are shown in Figure 7A, together with a composite spectrum compared with the experimental total absorbance. The difference between the first inflection energies of the octahedral and tetrahedral sites is approximately 2eV. Figure 7B shows the composite DAFS-extracted EXAFS oscillations, compared with the EXAFS from the absorbance. Examination of the site specific edge data shown in Figure 7A allows us to assign individual features of the total X-ray absorption edge spectrum to tetrahedral and octahedral sites, and this is shown in Figure 8. Figure 9 shows the DAFS-extracted EXAFS and corresponding Fourier transforms for the two different cobalt sites, compared with calculations based on the crystal structure [26]. Taken together, these data provide compelling evidence that DAFS can readily provide site specific X-ray absorption spectra.

The site specific Co_3O_4 cobalt K-edge spectra provide some interesting insights. Lenglet et al. [28] have examined the Co K-edge X-ray absorption spectra for a number of spinels and inverse spinels, and Sano [29], and later Briois et al. [30], have examined a wide range of Co(II) and Co(III) compounds with different coordination environments. For an octahedral cobalt site we expect the spectrum to be dominated by a pronounced $1s{\rightarrow}4p$ transition at about 7730eV [30], which is intense because of the degeneracy of the $4p$ levels in an octahedral environment. The $1s{\rightarrow}3d$ transition at about 7711eV should be very weak as in O_h symmetry no mixing of the metal $4p$ levels is expected, and the transition is thus dipole forbidden. The transition gains small (but significant) intensity from being quadrupole allowed and possibly dipole-allowed intensity from $3d$-$4p$ mixing due to vibronic interactions [31]. In agreement with this, the spectrum in Figure 7 shows a pronounced peak at 7730eV, and no detectable $1s{\rightarrow}3d$ pre-edge peak. For tetrahedral cobalt, on the other hand, we expect a more pronounced $1s{\rightarrow}3d$ transition as mixing of metal $4p$ with the t_2 d-orbitals is expected [cf. 24], and this was observed by Briois et al. [30]. Unfortunately the signal to noise of the DAFS-extracted XAFS, combined with the resolution of the Si(111) monochromator used for this experiment, prevents us from definitively observing this feature, although there may be a small peak at 7710eV (Figure 7). For tetrahedral cobalt, no pronounced $1s{\rightarrow}4p$ transition, such as that observed for the octahedral sites, is expected because of the mixing with metal $3d$ orbitals [30]. We observe three features in the tetrahedral spectrum, at X-ray energies 7719.6 eV, 7724.3 eV and 7737.7 eV. Lenglet et al. [28] have examined the Co K-edge spectra of the spinel $CoRh_2O_4$, which contains only tetrahedral cobalt, and observe a more pronounced $1s{\rightarrow}3d$ transition than for octahe-

dral complexes, and three features in the edge which correspond closely with those observed for the tetrahedral site of Co_3O_4.

In the case of a spinel structure such as Co_3O_4 we have advantageous spacegroup absences for the two cations, so that the contributions can be separated completely by choosing just two peaks. The more general case is that all anomalous atoms would contribute to all Bragg peaks [32], and therefore a direct separation of this nature does not occur since the $f_m{'}(E)$ and $f_m{''}(E)$ of Equation 7 are weighted mean values of all the atoms. However, different anomalous atom types will contribute to the peaks with varying proportions, and therefore, with a knowledge of the crystal structure, indirect separation will be possible with careful combination of the data from n-1 (or more) diffraction peaks, and absorbance, where n equals the number of distinct anomalous atoms.

Polarized Diffraction Anomalous Fine Structure of $K_2Ni(CN)_4$. A valuable route to assigning features in an X-ray absorption edge spectrum, and therefore to interpreting them in terms of the electronic structure, is to obtain polarized XAFS spectra. A polarized X-ray absorption edge study of a single crystal of $K_2Ni(CN)_4 \cdot H_2O$ has been reported by Kosugi *et al.* [33]. Unfortunately, no crystal structure data has been reported for this compound, and the interpretation of the spectroscopic results was based on speculation that planar $[Ni(CN)_4]^{2-}$ anions are oriented perpendicular to a particular (unspecified) crystal cleavage plane. The crystal structure of the anhydrous form, $K_2Ni(CN)_4$, however, has been determined using a combination of powder and single crystal X-ray diffraction [34]. Because of this, and because of the tendency of $K_2Ni(CN)_4 \cdot H_2O$ to lose water of crystallization, we chose to study the polarized DAFS of $K_2Ni(CN)_4$. The space group of $K_2Ni(CN)_4$ is $P2_1/c$, and the structure consists of two sets of isolated square-planar *(D_{4h}* symmetry) $[Ni(CN)_4]^{2-}$ anions with planes inclined at 18.55° to each other, and at 80.73° to the (010) plane [34]. Figure 10 shows the Ni K-edge spectrum of $K_2Ni(CN)_4$, together with the crystal structure (inset) viewed down the crystallographic *a*-axis. We also recorded the powder XAFS spectrum of $K_2Ni(CN)_4 \cdot H_2O$ (not illustrated), and found that both the Ni K-edge EXAFS and the edge spectrum were essentially identical to that of $K_2Ni(CN)_4$. Very similar powder Ni K-edge spectra were obtained for $K_2Ni(CN)_4 \cdot H_2O$ by Kosugi *et al.* [33], and we conclude that the local environment of the nickel in these compounds is identical. In polarized single crystal measurements, Kosugi *et al.* [33] found that the prominent pre-edge features A at 8335.3eV and B at 8343.5eV (see Figure 10)

are strongly anisotropic, being most intense for the e-vector orientation assumed to be normal to the $[Ni(CN)_4]^{2-}$ plane. The broad feature C was found to be less anisotropic, with opposite sense [33].

We were able to collect several diffraction peaks of interest for polarized DAFS of $K_2Ni(CN)_4$ in the same energy scan since they lie within a small range of d-spacings. Figure 11 shows the Bragg scan for a single energy point in a DAFS scan which includes five prominent diffraction peaks, together with the minimized pseudo-Voigt function which was used to extract the integrated intensities. As was noted above, we expect a dipole allowed transition in powder DAFS to have an intensity, I, relative to the powder, given by $I=(3\sin^2\zeta)/2$, where ζ is the angle between the transition dipole vector and the normal to the hkl plane (in other words the angle between the Bragg plane and the $[Ni(CN)_4]^{2-}$ plane). The DAFS-extracted Ni K-edge X-ray absorption edge spectra for the (020), (100), (11$\bar{1}$), (013), (102) and (10$\bar{2}$) Bragg reflections are shown in Figure 12. It can be seen that the intensity of both the pre-edge feature A and the shoulder B vary as the reflection is changed, with the broad feature C showing a more subtle variation. The area of the pre-edge peak A was measured by fitting the spectra to an edge jump function plus a sum of pseudo-Voigt peaks to approximate the spectral structure [27]. In Figure 13, the peak areas thus obtained are plotted against the calculated value of $(3\sin^2\zeta)/2$ averaged over the two $[Ni(CN)_4]^{2-}$ orientations in the unit cell, assuming a transition dipole vector oriented normal to the $[Ni(CN)_4]^{2-}$ plane. The points clearly describe a straight line, and, in agreement with the conclusions of Kosugi et al. [33] we find that the intensity of the peak A is maximal when the e-vector is perpendicular to the $[Ni(CN)_4]^{2-}$ plane. Also in agreement with Kosugi et al. [33], it can be seen from Figure 12 that a similar polarization dependence is observed for the peak B, while the broader feature C shows a much smaller angular dependence, of opposite sign.

The $[Ni(CN)_4]^{2-}$ anion is often used as an example of a typical square planar Ni^{2+} complex [e.g. 35], and its electronic structure has been the subject of some investigation [e.g. 36,37]. The resonance C is perhaps the most readily assigned, a very similar structure being observed for $[Co(CN)_6]^{3-}$ [29], for $[Fe(CN)_6]^{3-}$ and $[Fe(CN)_6]^{4-}$ [38] and for $[Fe(CN)_5NO]^{2-}$ [39]. In the case of $[Co(CN)_6]^{3-}$ [29] molecular orbital calculations have been used to assign a $1s \rightarrow t_{1u}$ (Co $4p$ - CN^- 6σ) transition, and it can be alternatively rationalized as a σ^* type shape-resonance set up by the cage of CN^- [38]. For $[Ni(CN)_4]^{2-}$ a σ^* shape-resonance would be ex-

pected to be have maximal intensity when the e-vector is in the $[Ni(CN)_4]^{2-}$ plane, and this is indeed the case for peak C (see Figure 10). The transitions A and B, on the other hand, are not observed in octahedral cyanide complexes, and these prove rather more problematic to assign. In square planar complexes, Ni^{2+} is low-spin $3d^8$ ($S=0$), and the planar ligand field causes the single unoccupied $3d_{x^2-y^2}$ orbital to be highest in energy. This orbital resides in the $[Ni(CN)_4]^{2-}$ plane, and we expect the lowest energy transition to be a weakly quadrupole allowed $1s \to 3d_{x^2-y^2}$ peak at about 8333eV [40], which should be most intense when the e-vector is in the $[Ni(CN)_4]^{2-}$ plane. The peak A at 8335.3eV is very close to the expected position for the $1s \to 3d$ peak, although it is far too intense, and of incorrect polarization to be the expected quadrupole-allowed $1s \to 3d$ peak. Kosugi et al. [33] have suggested that A and B are due to transitions to metal $4p\pi^*$ orbitals with large mixing with $CN^- 2\sigma^*$ components; however A is too close to the $1s \to 3d$ to be due to transitions to the predominantly metal based $4p_z$ orbital. One possibility which must be considered is that π back-bonding from the filled metal $3d$-orbitals to CN^- based $2\pi^*$ orbitals allows us to observe a $1s \to 3d$ π^* transition. However, the cyanide ion is generally considered to be a good σ electron donor and a poor π electron acceptor [35], and, in agreement with this, molecular orbital calculations suggest that there is little ligand π back-bonding [36,37]. Square planar Cu^{2+} complexes have been much studied, and also possess pronounced z-polarized low energy transitions, although at a higher energy relative to the $1s \to 3d$ transition (~8eV, compared to ~2.5eV for peak A of $K_2Ni(CN)_4$). These transitions are thought to be $1s \to 4p_z$ + ligand to metal charge transfer shake-down transitions [41-44]. It is possible that the peaks A and B in the $[Ni(CN)_4]^{2-}$ edge spectra are due to similar multielectron shake-down events; however, a final conclusion must await the results of a more detailed theoretical analysis.

Discussion

The results presented in this paper demonstrate that DAFS is a fundamentally viable technique for probing the structure of a variety of samples. Information can be obtained which is not available using XAFS and X-ray diffraction separately. All of the results presented are of dilute powder materials, and acceptable quality data was obtained, despite the very much lower diffracted intensity in powders compared with the corresponding single crystal case.

We have demonstrated in this paper an iterative method for deconvolving the real

and imaginary components of the anomalous scattering factor from the DAFS signal. There are two major advantages of our procedure for DAFS data reduction. The first is that the method can be applied to obtain local structural information for any crystalline material without *a priori* knowledge of its structure. A corollary of the method is that in solving for the various constants we also obtain phase information for the anomalous atom under investigation (*e.g.* values of α/A) which could assist in full crystal structure determination for an unknown. A second advantage of our methodology is that the final result of the analysis procedure is an absorbance spectrum. Direct comparison between DAFS spectra or of a DAFS spectrum with an XAFS spectrum may be uninformative, due to varying (possibly unknown) proportions of $f'(E), f''(E)$ and their respective squared terms, depending on the structure factor of the particular reflection. In the case of the DAFS-extracted XAFS these comparisons can indeed be made, in both the EXAFS and the edge spectra. In the case of the EXAFS, an important advantage is that the spectrum can then be analyzed by traditional curve-fitting methods, using widely available EXAFS phase and amplitude functions [*e.g.* 23].

As stated above, all of the experiments described herein are of powders. Powder diffraction has recently gained increased importance due to its application to crystal structure determination of materials for which single crystals are unavailable [*e.g.* 45 and refs. therein, 46]. Polycrystalline powder samples of this type represent a very substantial group of materials, many of which are of great importance. In addition to the local, site specific, structural XAFS information discussed above, DAFS provides substantial phase information which could assist in structure determination. Indeed, in the future it may prove possible to co-refine diffraction intensities and the DAFS oscillations, which would exploit the (often) higher resolution afforded by EXAFS. The use of DAFS to characterize components of mixtures has applications in many disciplines including heterogeneous catalysis and mineralogy, where DAFS could help to locate an element in a particular component, and deduce its respective local structure. Furthermore, using DAFS, polarized XAFS can be obtained from powders, as has been demonstrated by our study of $K_2Ni(CN)_4$, and has the ability to give similar information to single crystal XAFS.

Another future application of DAFS is with single crystal diffraction. From the point of view of signal to noise, single crystal DAFS is experimentally easier than for powders [*cf* 10]. Different diffraction peaks can be used to selectively probe the polarized XAFS of crys-

tallographically distinct occurrences of the same element. This could be of importance, for example, in the determination of active sites in single crystals of metalloproteins. In this case, the location of a particular metal may be crystallography located to low resolution, at best to tenths of an Ångström. The precise site coordination, and hence oxidation state, which is of critical importance for elucidating the nature of the active site, cannot always be determined from the crystallography alone. Bulk XAFS, similarly, can only give an average over all occurrences of the element in the structure. In contrast, DAFS has the potential to selectively probe the coordination geometry of individual sites, and moreover, exploiting the polarized nature of synchrotron radiation, could be used to deduce the spatial orientation of individual sites within the crystal.

References:

(1) (a) Lye, R.C.; Phillips, J.C.; Kaplan, D.; Doniach, S.; Hodgson, K.O. *Proc. Natl. Acad. Sci. U.S.A.* **1980**, *77*, 5884-5888. (b) Guss, J.M.; Merritt, E.A.; Phizackerley, R.P.; Hedman, B.; Murata, M.; Hodgson, K.O.; Freeman, H.C. *Science*, **1988**, *241*, 806-811. (c) Karle, J. *Physics Today*, **1989**, 22-29. (d) Hendrickson, W.A. *Science* **1991**, *254*, 51-58.

(2) (a) Bonse, U.; Hartman-Lotsch, I. *Nucl. Instrum. Meth.* **1984**, *222*, 185-188. (b) Templeton, D.H.; Templeton, L.K. *Acta. Cryst.* **1982**, *A38*, 62-67. (c) Arcon, I.; Kodre, A.; Hribar, M. *in X-ray Absorption Fine Structure (Hasnain, S.S. Ed., Publisher: Ellis Horwood)* **1991** 726-728.

(3) Arcon, I.; Kodre, A.; Glavic, D.; Hribar, M. *J. de Physique* **1987**, *C9*, 1105-1108.

(4) Attfield, J.P. *Nature*, **1990**, *343*, 46-49.

(5) Wilkinson, A.P.; Cox, D.E.; Cheetham, A.K. *Acta. Cryst.* **1991**, *B47*, 155-161.

(6) (a) Kwei, G.H.; Von Dreel, R.B.; Williams, A.; Goldstone, J.A.; Lawson II, A.C.; Warburton, W.K. *J. Mol. Struct.* **1990**, *223*, 383-406. (b) Attfield, J.P. *J. Phys. Chem. Solids* **1991**, *52*, 1243-1249.

(7) Wilkinson, A.P.; Cox, D.E.; Cheetham, A.K. *J. Phys. Chem. Solids* **1991**, *52*, 1257-1266.

(8) (a) Ponomarev, Yu.V.; Turutin, Yu.A. *Sov. Phys. Tech. Phys.* **1983**, *28*, 1474. (b) Ponomarev, Yu.V.; Turutin, Yu.A. *Sov. Phys. Tech. Phys.* **1984**, *29*, 232-234.

(9) Pickering, I.J.; Sansone, M.; Marsch, J.; and George, G.N. *Japan J. Appl. Phys.* **1992** (in the press)

(10) Stragier, H.; Cross, J. O.; Rehr, J. J.; Sorensen, L. B.; Bouldin, C. E.; Woicik, J. C. *Phys. Rev. Lett.* **1992**, *69*, 3064-3067.

(11) Fernelius, W. C. and Burbage, J. J. **1946**, *Inorganic Syntheses Vol. II* (McGraw-Hill

Book Company, N.Y.), p.227.

(12)   The National Synchrotron Light Source is funded by the Division of Materials Sciences, U.S. Department of Energy, under contract DE-AC02-76CH-0016.

(13)   Sansone, M.; Via, G.; George, G.N.; Meitzner, G.; Hewitt, R. *in X-ray Absorption Fine Structure (Hasnain, S.S. Ed., Publiser: Ellis Horwood)* **1991** 656-658.

(14)   Sansone, M. *in National Synchrotron Light Source Annual Report* **1991**, *1*, 96.

(15)   Goulon, J.; Goulon-Ginet, C.; Cortes, R.; Dubois, J.M. *J. Physique* **1982**, *43*, 539-548.

(16)   Sparks, C.J. Jr. *Phys. Rev. Lett.* **1974**, *33*, 262-265.

(17) $\phi_r = hx_r + ky_r + lz_r$, where h, k, l are the Miller indices of the diffraction peak and x_r, y_r and z_r are the fractional unit cell coordinates of the atom r.

(18)   The scattering factor f_T incorporating the temperature factor B may be expressed as $f_T = f_r \exp(-B\sin^2\theta/\lambda^2)$, where λ is the wavelength of the incident X-rays, and $B = 8\pi^2\overline{u^2}$, where $\overline{u^2}$ is the mean square displacement of the atom. The function $\sin^2\theta/\lambda^2$ is a constant for a given diffraction peak scanned in the manner described, and therefore if isotropic thermal motion can be assumed, the temperature factor reduces to a constant.

(19)   Since $(A^2 + B^2)(\alpha^2 + \beta^2) = (A\alpha + B\beta)^2 + (B\alpha - A\beta)^2$, there are only 3 independent coefficients in Equation 6.

(20)   (a) Cromer, D.T.; Liberman, D. *Acta Cryst.* **1981** *A37*, 267-268. (b) Cromer, D. *J. Appl. Cryst.* **1983**, *16*, 437. (*Note:* The program of Cromer was modified as recommended by D.C.Creagh, to correct errors in the original)

(21)   Templeton, L.K.; Templeton, D.H. *J. Appl. Cryst.* **1988**, *21*, 558-561.

(22)   (a) Peterson, C.W.; Knight, B.W. *J. Opt. Soc. Amer.* **1973**, *63*, 1238-1242. (b) Johnson, D.W. *J. Phys. A: Math. Gen.*, **1975**, *8*, 490-495.

(23)   (a) Rehr, J.J.; Mustre de Leon, J.; Zabinsky, S.I.; Albers, R.C. *J. Amer. Chem. Soc.* **1991**, *113*, 5135-5140. (b) Mustre de Leon, J.; Rehr, J.J.; Zabinsky, S.I.; Albers, R.C. *Phys. Rev. B*, **1991**, *44*, 4146-4156.

(24)   Kutzler, F.W.; Natoli, C.R.; Misemer, D.K.; Doniach, S.; Hodgson, K.O. *J. Chem. Phys.* **1980**, *73*, 3274-3288.

(25)   International Tables for X-ray Crystallography, **1989**, *Volume A*, (Ed. Theo Hahn, Kluwer Academic Publishers)

(26)   Knop, O.; Reid, K.I.G. *Can. J. Chem.* **1968**, *46*, 3463-3476.

(27)   Edge spectra were fitted to a sum of pseudo-Voigt peaks, plus a function designed to approximate the edge step {*cf.* Stöhr, J. *NEXAFS Spectroscopy*, Springer Verlag **1992**, Chapter 7.}. The powder data were first fitted, and the positions of all peaks were then held fixed while fitting the DAFS-extracted XAFS data.

(28)   Lenglet, M.; D'Huysser, A.; Dürr, J. *Ann. Chim. Fr.* **1988**, *13*, 505-515.

(29)   Sano, M. *Inorg. Chem.* **1988**, *27*, 4249-4253.

(30)   Briois, V.; Cartier, C.; Momenteau, M.; Maillard, Ph.; Zarembowitch, J.; Dartyge, E.; Fontaine, A.; Tourillon, G.; Thuéry, P.; Verdaguer, M. *J. de Chimie Phys.* **1989**, *86*, 1623-1634.

(31)   Hahn, J.E.; Scott, R.A.; Hodgson, K.O.; Doniach, S.; Desjardins, S.R.; Solomon, E.I. *Chem. Phys. Lett.* **1982**, *88*, 595-598.

(32)   Such a case has recently been investigated by Stragier, Sorenson, Bouldin and co-workers (personal communication), who have performed a detailed study of the DAFS of an epitaxial thin film of $YBa_2Cu_3O_{7-\delta}$.

(33)   Kosugi, N.; Yokoyama, T.; Kuroda, H. *Chem. Phys.* **1986**, *104*, 449-453.

(34)   Vannerberg, N.-G. *Acta Chem. Scand.* **1964**, *18*, 2385-2391.

(35)   Cotton, A.F.; Wilkinson, G. *Advanced Inorganic Chemistry*, John Wiley & Sons,

1988, *Fifth Edition*, pp 743-747.

(36)   Hillier, I.H.; Saunders, V.R. *Mol. Phys.* **1972**, *23*, 449-456.

(37)   Demuynck, J.; Veillard, A. *Theoret. Chim. Acta (Berl.)* **1973**, *28*, 241-265.

(38)   Bianconi, A.; Dell'Ariccia, M.; Durham, P.J.; Pendry, J.B. *Phys. Rev. B* **1982**, *26*, 6502-6508.

(39)   Gädeke, W.; Koch. E.E.; Dräger, G.; Frahm, R.; Saile, V. *Chem. Phys.* **1988**, *124*, 113-119.

(40)   We estimate an expected $1s \rightarrow 3d$ energy of 8333eV from the average value of nickel K-edge spectra from a large number of Ni^{2+} compounds.

(41)   Bair, R.A.; Goddard, W.A. *Phys. Rev. B* **1980**, *22*, 2767-2776.

(42)   Kosugi, N.; Yokohama, T.; Asakura, K.; Kuroda, H. *Chem. Phys.* **1984**, *91*, 249-256.

(43)   Smith, T.A.; Penner-Hahn, J.E.; Berding, M.A.; Doniach, S.; Hodgson, K.O. *J. Amer. Chem. Soc.* **1985**, *107*, 5945-5955.

(44)   Yokoyama, T.; Kosugi, N.; Kuroda, H. *Chem. Phys.* **1986**, *103*, 101-109.

(45)   Cheetham, A.K.; Wilkinson, A.P. *J. Phys. Chem. Solids* **1991**, *52*, 1199-1208.

(46)   Morris, R.E.; Harrison, W.T.A.; Nicol, J.M.; Wilkinson, A.P.; Cheetham, A.K. *Nature* **1992**, *359*, 519-522.

Figure captions:

Figure 1. Diagram of the experimental setup for a DAFS experiment.

Figure 2. Example of experimental output of a single DAFS scan of a sample of 5wt. % $KMnO_4$ in Li_2CO_3.

A. The $KMnO_4$ (211) diffraction peak scanned with different incident X-ray energies in the vicinity of the manganese X-ray absorption K-edge. The intensity variation in the peak intensity, from which the DAFS signal is extracted, can be clearly seen. In addition, structure from the small amount of X-ray fluorescence (mainly Mn K_β) included in the scatter single channel analyzer window, can be seen as increased background.

B. a. The raw (211) DAFS spectrum of $KMnO_4$. *b.* The raw DAFS spectrum (as in *a.* but with bulk absorption and Lorentz corrections applied). *c.* The XAFS of $KMnO_4$ (for comparison), measured by conventional transmittance simultaneously with the DAFS scan.

Figure 3. Example of the results of applying the iterative method of data analysis to extract a XAFS spectrum from a raw DAFS spectrum of 5wt. % $KMnO_4$ in Li_2CO_3.

A. $f''(E)$ *(a)* and $f'(E)$ *(b)* functions for $KMnO_4$. The solid lines show the functions as extracted from the DAFS data. The broken lines show the starting functions used in the data analysis which correspond to the Cromer Liberman theory curves, convoluted with a pseudo-Voigt function and shifted by an appropriate energy. The inset in *A* shows an Argand diagram of the anomalous correction. Note the large epicyclic feature which corresponds to the *1s→3d* transition at 6543.2eV.

B. A comparison of the normalized absorbance extracted from the $KMnO_4$ (211) DAFS *(b)* with the XAFS spectrum *(a)*.

Figure 4. Separation of DAFS from a mixture of phases. The sample is 2 wt.% each of Cr_2O_3 and Na_2CrO_4 in PVPP. For this experiment, the diffracted beam vertical collimating slits were opened to 3mm and five data points per energy step were collected, one at the maximum intensity of each of two Bragg peaks and three background points.

Data is from a single scan of *ca.* $3^1/_4$ hours. *(a)* The absorbance of the mixture. *(b)* and *(d)* show the DAFS-extracted XAFS of Na_2CrO_4 (031) and Cr_2O_3 (104), respectively. *(c)* and *(e)* are the XAFS spectra of pure Na_2CrO_4 and Cr_2O_3, respectively, recorded independently of the DAFS experiment.

Figure 5. Powder diffraction patterns recorded for a mixture of Co_3O_4 in Li_2CO_3 at three different energies as shown. The patterns are plotted as a function of $Q = 2\pi/d = 4\pi\sin\theta/\lambda$. A large anomalous effect is seen for the Co_3O_4 (222) diffraction peak, which has close to zero intensity at the absorption edge of cobalt.

Figure 6. Raw DAFS spectra for 5 wt.% Co_3O_4 in Li_2CO_3, shown after removal of bulk absorption and angular contributions. Spectra are shown for the (422) and (222) diffraction peaks of Co_3O_4, corresponding to the tetrahedral and octahedral cobalt, respectively, and the $(\bar{1}12)$ peak of Li_2CO_3, which was measured as a control (see text).

Figure 7. *A.* Cobalt K-edge X-ray absorption spectra for Co_3O_4. The bottom traces show the individual DAFS-extracted XAFS for the octahedral and tetrahedral cobalt sites. The top traces show the weighted sum ($^2/_3$ octahedral + $^1/_3$ tetrahedral) of the DAFS-extracted XAFS (broken line) compared with the bulk absorbance (solid line).

B. The k^2-weighted cobalt K-edge EXAFS from the absorbance (solid line) compared with the weighted sum of the DAFS-extracted EXAFS (broken line) for the two sites in Co_3O_4.

Figure 8. Co_3O_4 cobalt K-edge spectrum (points), together with the results of a curve-fitting analysis (solid line) *A*, and the corresponding second derivatives, *B*. The results of the curve-fitting are summarized by the stick diagram in *A*, and show the assignment of transitions to the tetrahedral (T_d) and octahedral (O_h) cobalt sites. The curve-fitting [27] yielded peak positions of 7709.9eV, 7713.7eV, 7719.6eV, 7724.3eV, 7730.0eV, 7737.7eV, 7744.4eV. The threshold (7733.3eV) was approximated by a single inflection, and was floated freely in the fit; because of the uncertainty concerning the actual position, we consider the amplitudes obtained to be ap-

proximate, especially for the 7737.7eV and 7744.4eV peaks.

Figure 9. Cobalt K-absorption edge DAFS-extracted EXAFS (A) and EXAFS Fourier transforms (B) for Co_3O_4. The solid lines show the DAFS-extracted EXAFS data for the (222) and the (422) diffraction peaks (octahedral and tetrahedral, respectively). The broken lines were calculated from the crystal structure for the individual sites.

Figure 10. The nickel K-absorption edge spectrum of powdered $K_2Ni(CN)_4$, together with the crystal structure viewed along the crystallographic a-axis (omitting the potassium ions for clarity). The columns of square planar $[Ni(CN)_4]^{2-}$ anions can be clearly seen.

Figure 11. A Bragg scan corresponding to a single energy point (8150eV) of the total DAFS scan for $K_2Ni(CN)_4$ (in this case each DAFS scan was comprised of more than 10^4 individual intensity measurements). The plot shows the experimental data as points, with the refined pseudo-Voigt profile which was used to extract the integrated intensity of the Bragg peaks. The mixing parameter of all pseudo-Voigt peaks was refined as a single common parameter, peak-widths, intensities and d-spacings were floated individually in the refinement, and the background was approximated using a low order polynomial. The lower solid line shows the residual of the fit.

Figure 12. DAFS-extracted Ni K-edge X-ray absorption spectra of $K_2Ni(CN)_4$ for the different diffraction peaks measured. From top to bottom, the (020), (102), (013), ($\bar{1}11$), (100) and ($10\bar{2}$) signals, in order of decreasing value of $\sin^2\zeta$.

Figure 13. The intensity of the 8335.3eV pre-edge peak A (see Figure 10) plotted against the mean value of $3(\sin^2\zeta)/2$, for the two $[Ni(CN)_4]^{2-}$ orientations in the unit cell, calculated from the crystal structure. ζ is the angle between the normal to the $[Ni(CN)_4]^{2-}$ square plane and the normal to the hkl diffraction plane. The average is over the two molecular orientation in the unit cell (normals to the molecular planes related by uvw and $u\bar{v}w$). An equivalent average is over the two sets of Bragg peaks which contribute intensity at a particular d-spacing. For this spacegroup, the reflections hkl and $h\bar{k}l$ generally have identical structure factors, but the presence

of anisotropy in the anomalous dispersion breaks this equivalence, and the computed average is over these two sets of reflections.
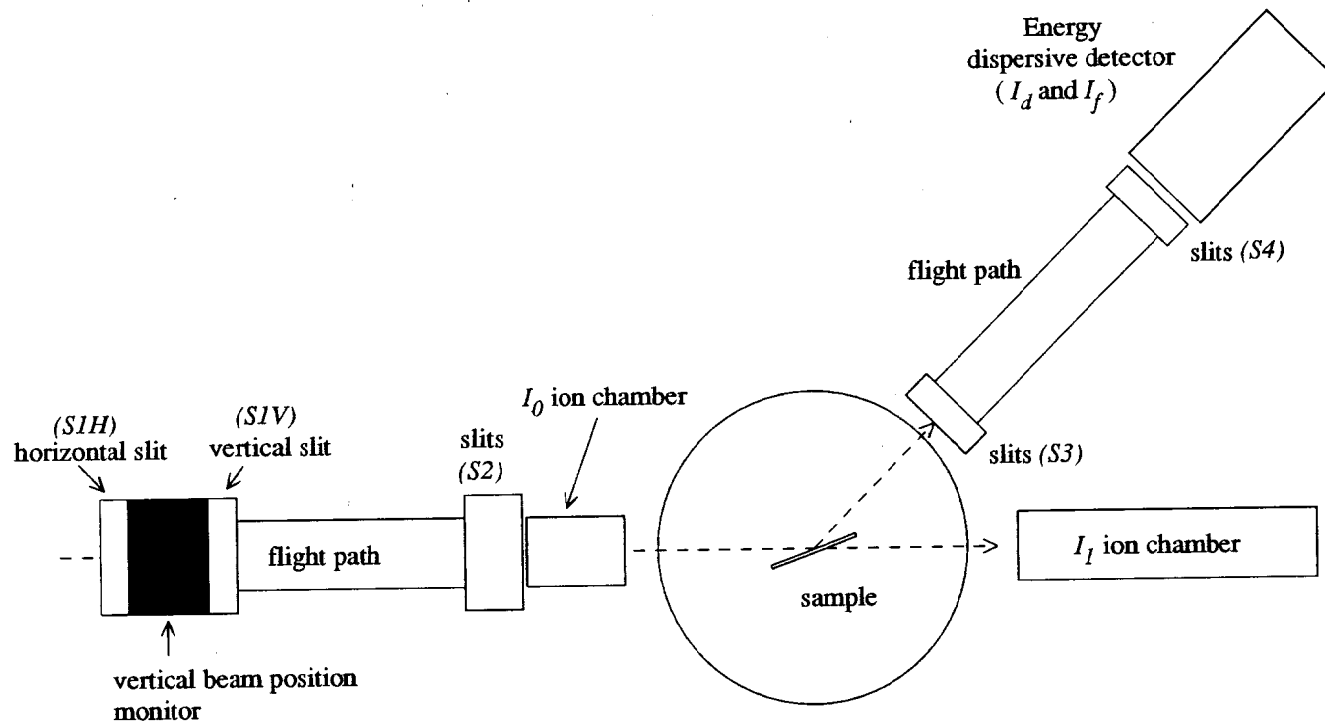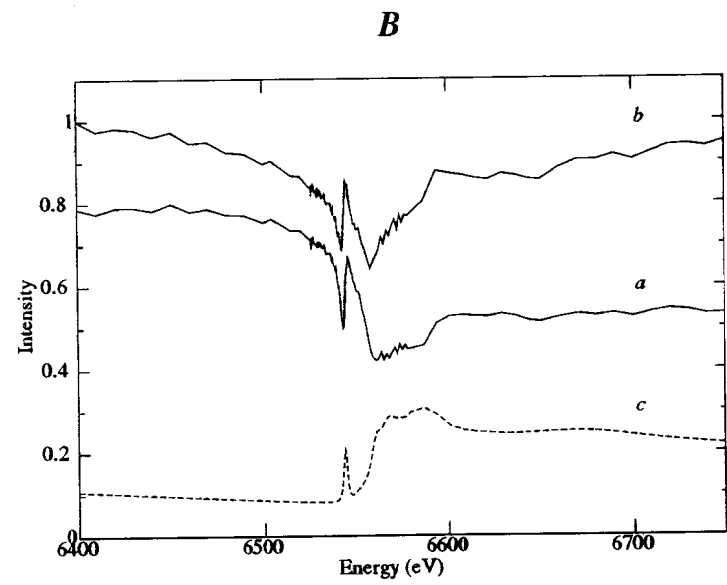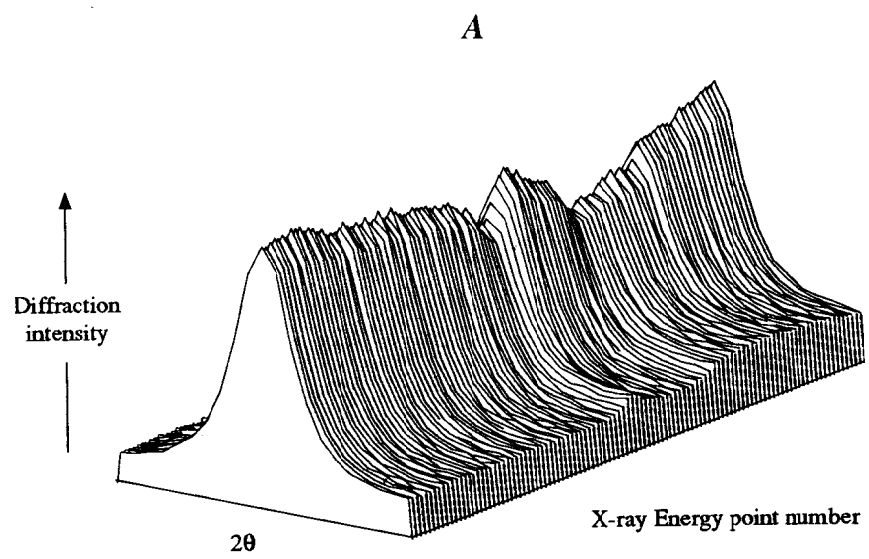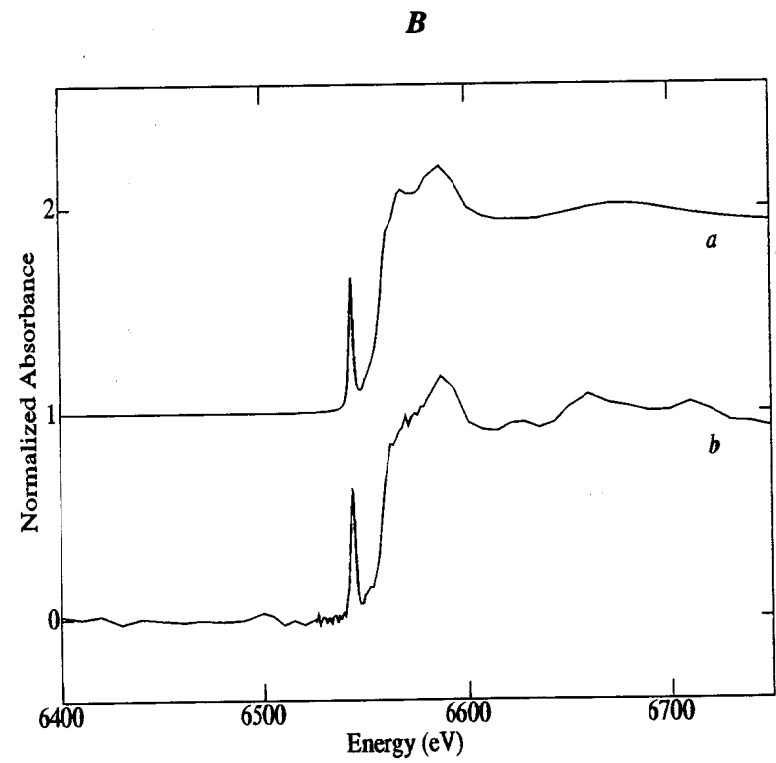
Energy
dispersive detector
(I_d and I_f)

slits *(S4)*

flight path

I_0 ion chamber

slits *(S3)*

(S1H)
horizontal slit

(S1V)
vertical slit

slits
(S2)

flight path

I_1 ion chamber

sample

vertical beam position
monitor

Figure 1

A

Diffraction intensity

2θ

X-ray Energy point number

B

Intensity

1

0.8

0.6

0.4

0.2

0

6400   6500   6600   6700

Energy (eV)

b

a

c

Figure 2

A
B
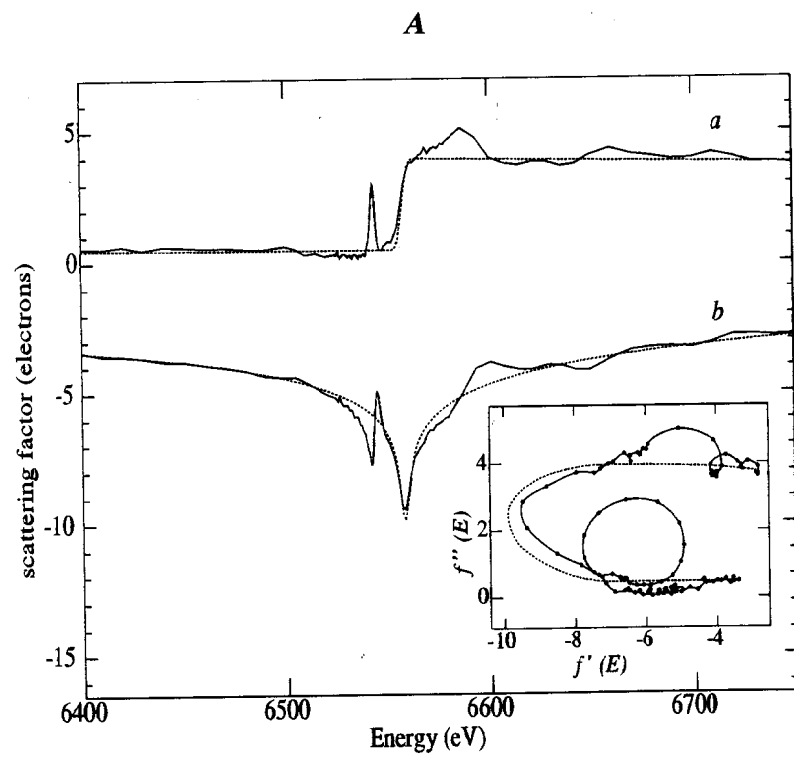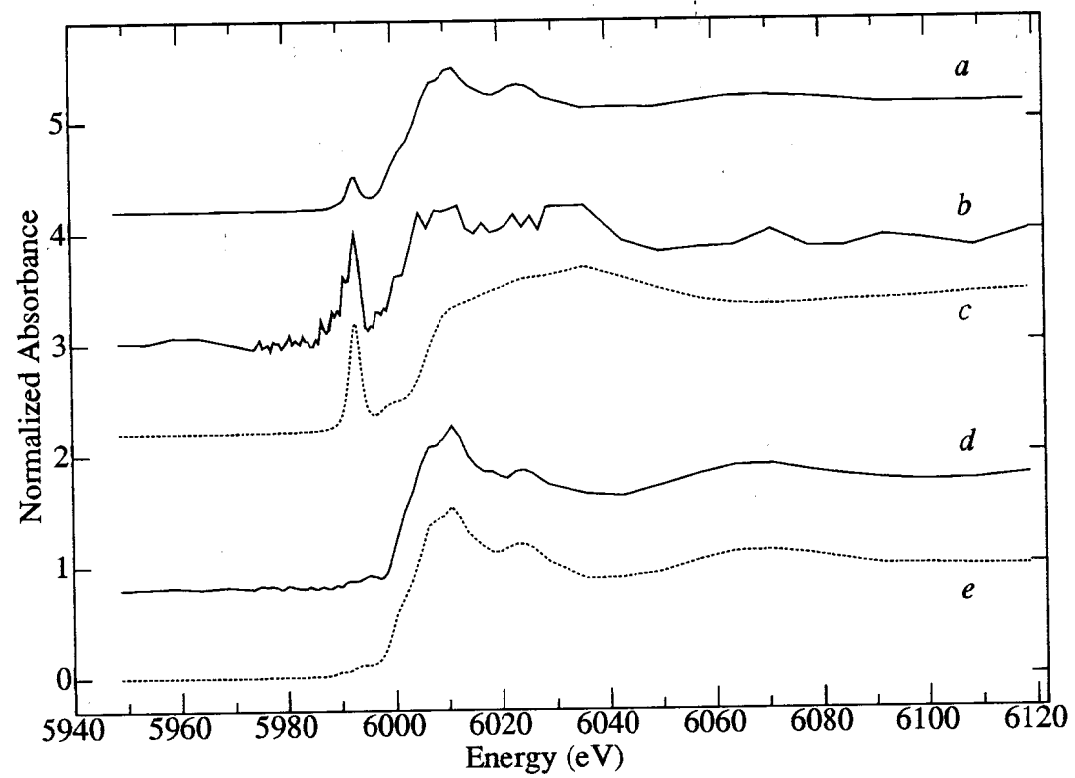
Figure 3

Figure 4

Figure 5

Figure 6

A

Normalized Absorbance

octahedral (222)

tetrahedral (422)
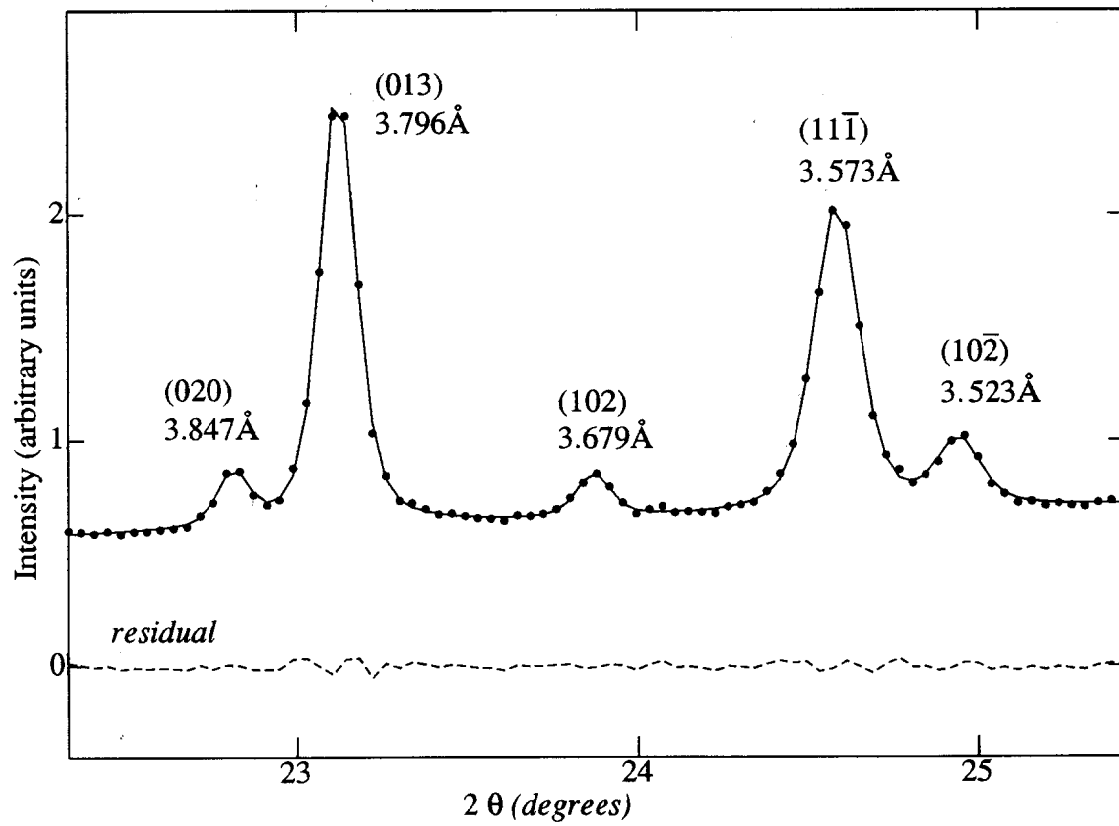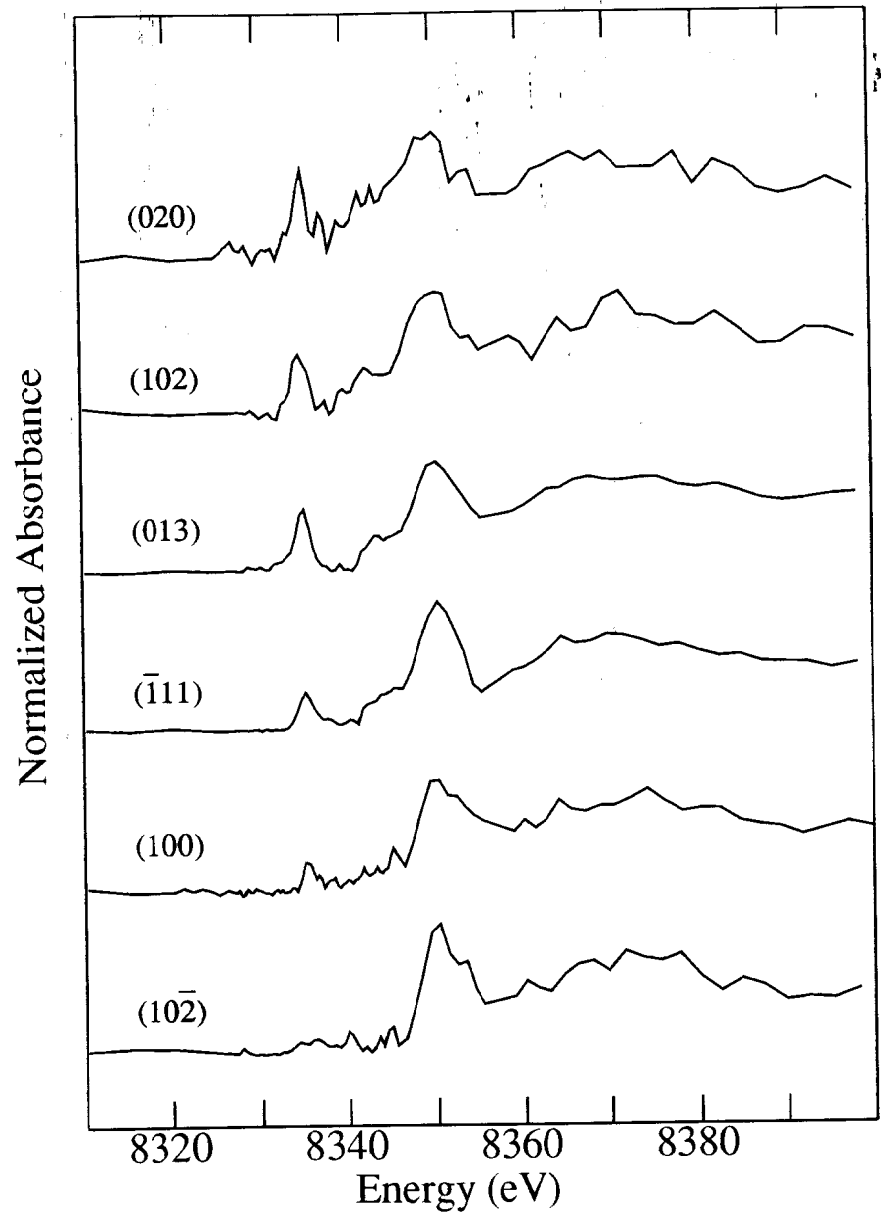
Energy (eV)

B

$\chi(k) \times k^2$
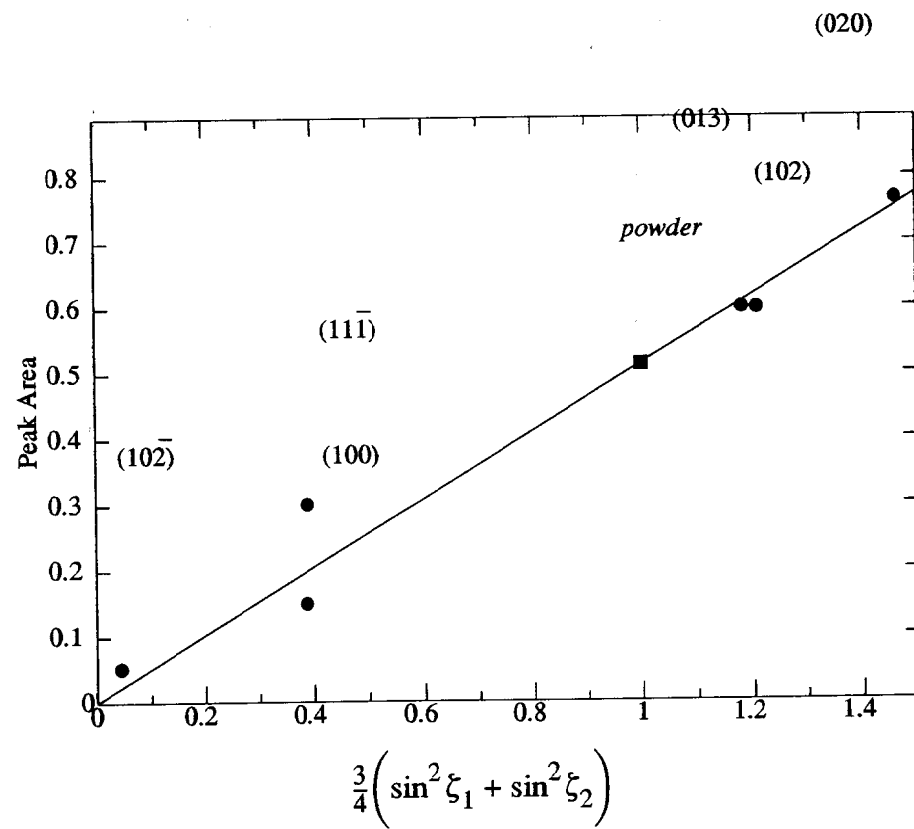
k (Å^{-1})
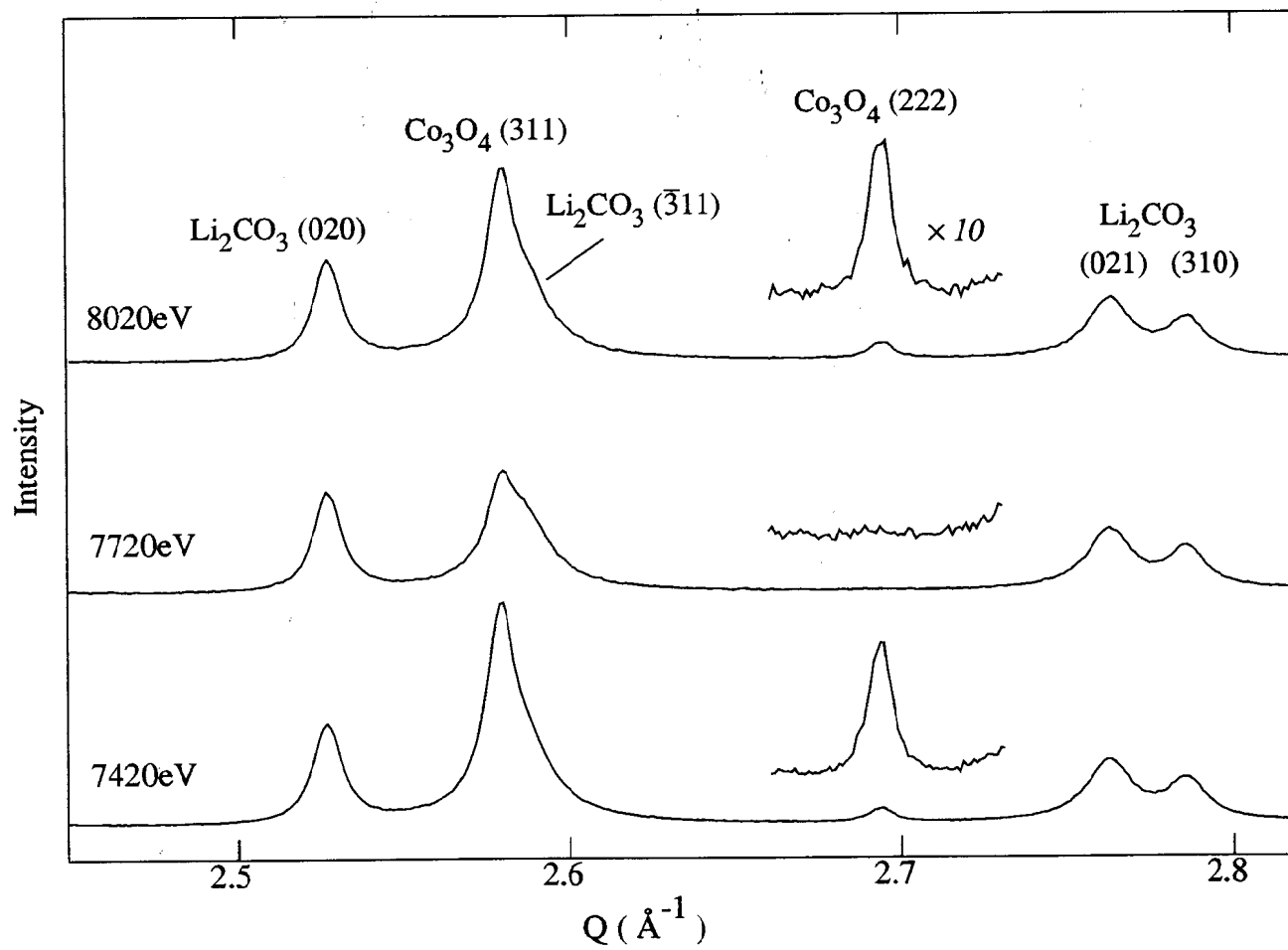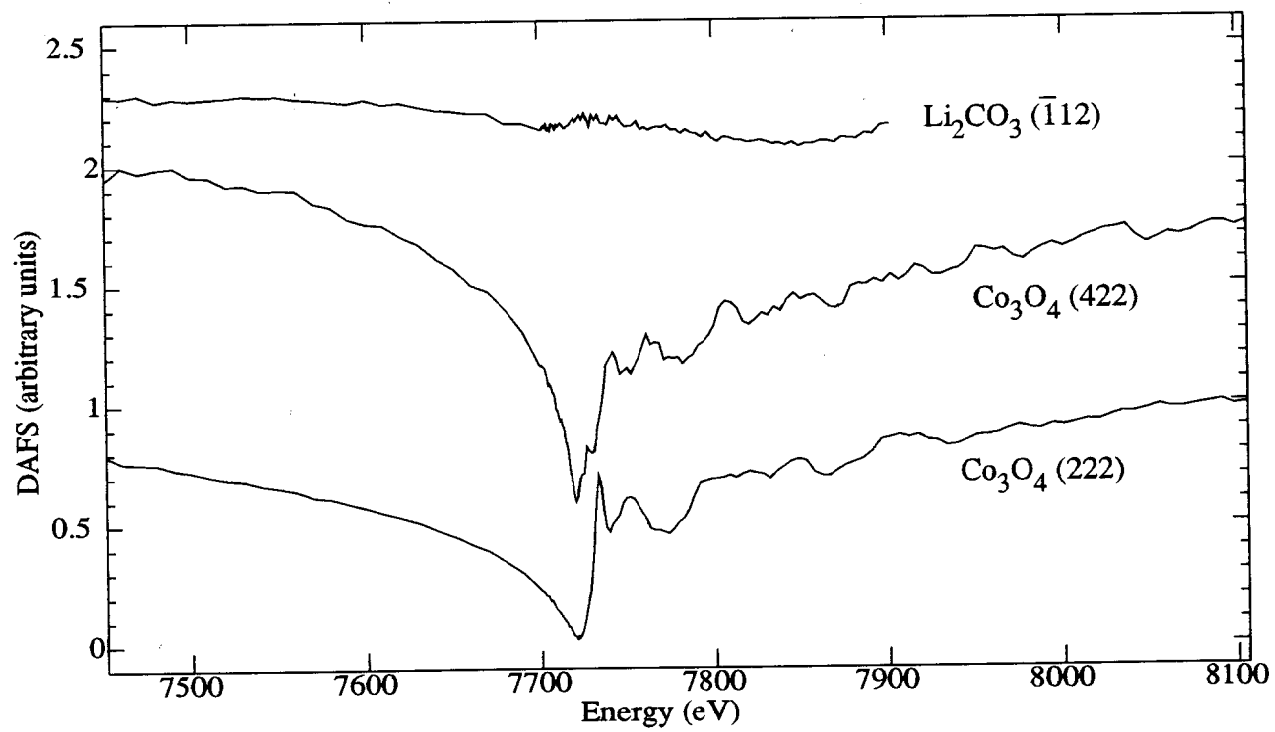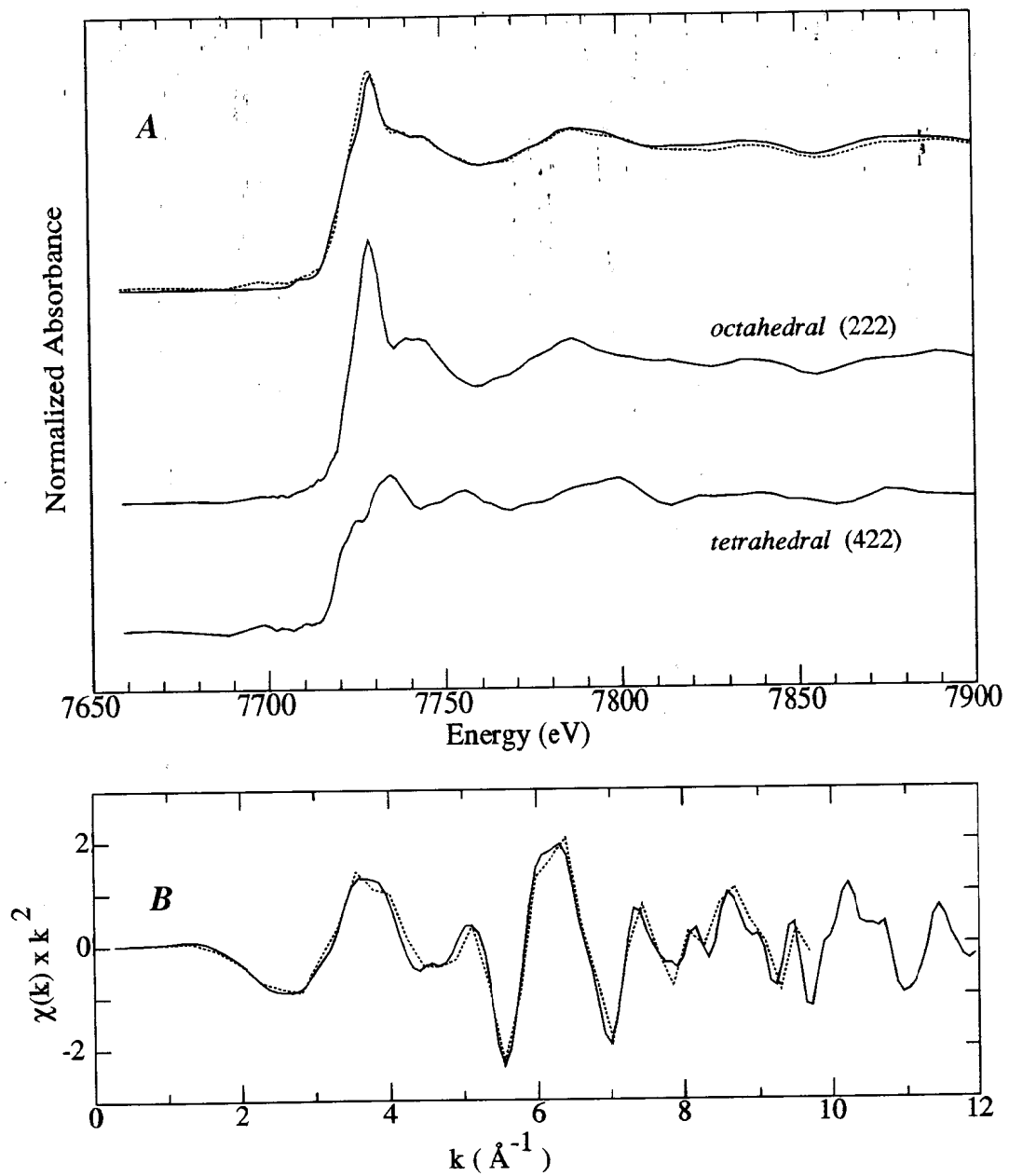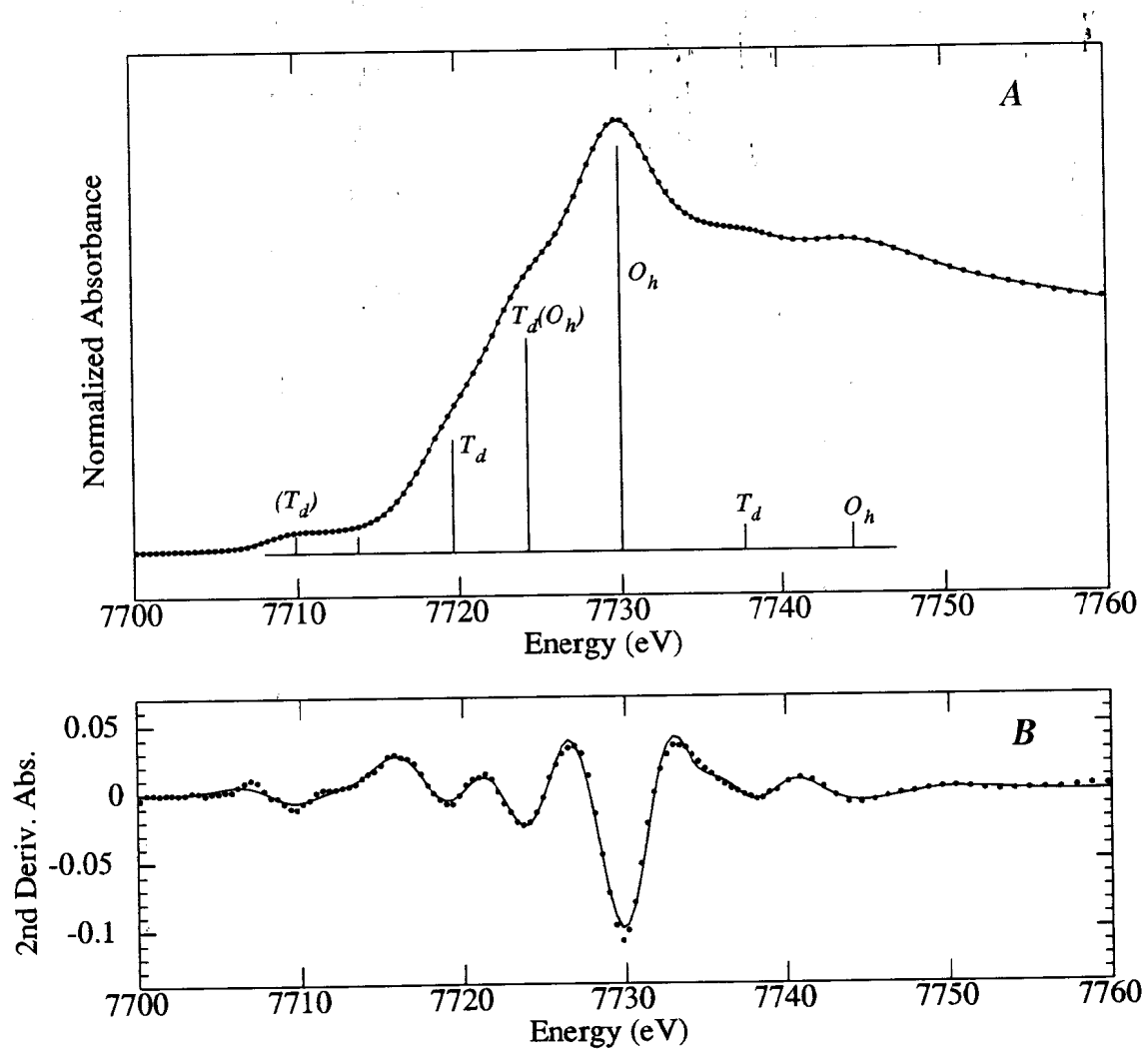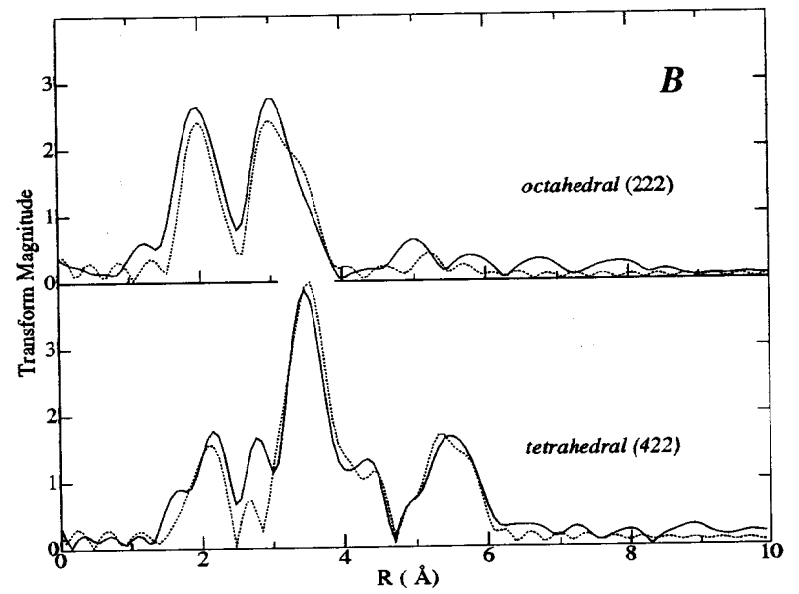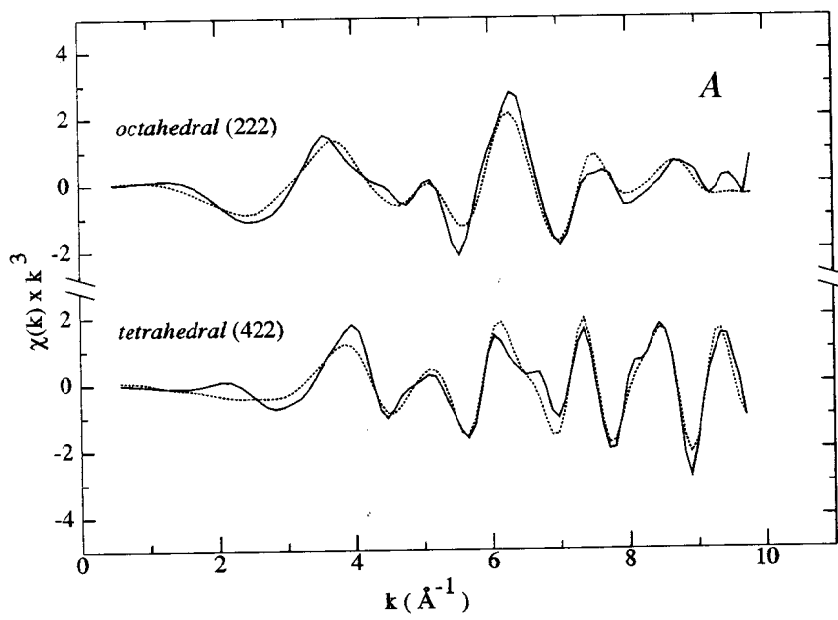
Figure 7

Figure 8

Figure 9
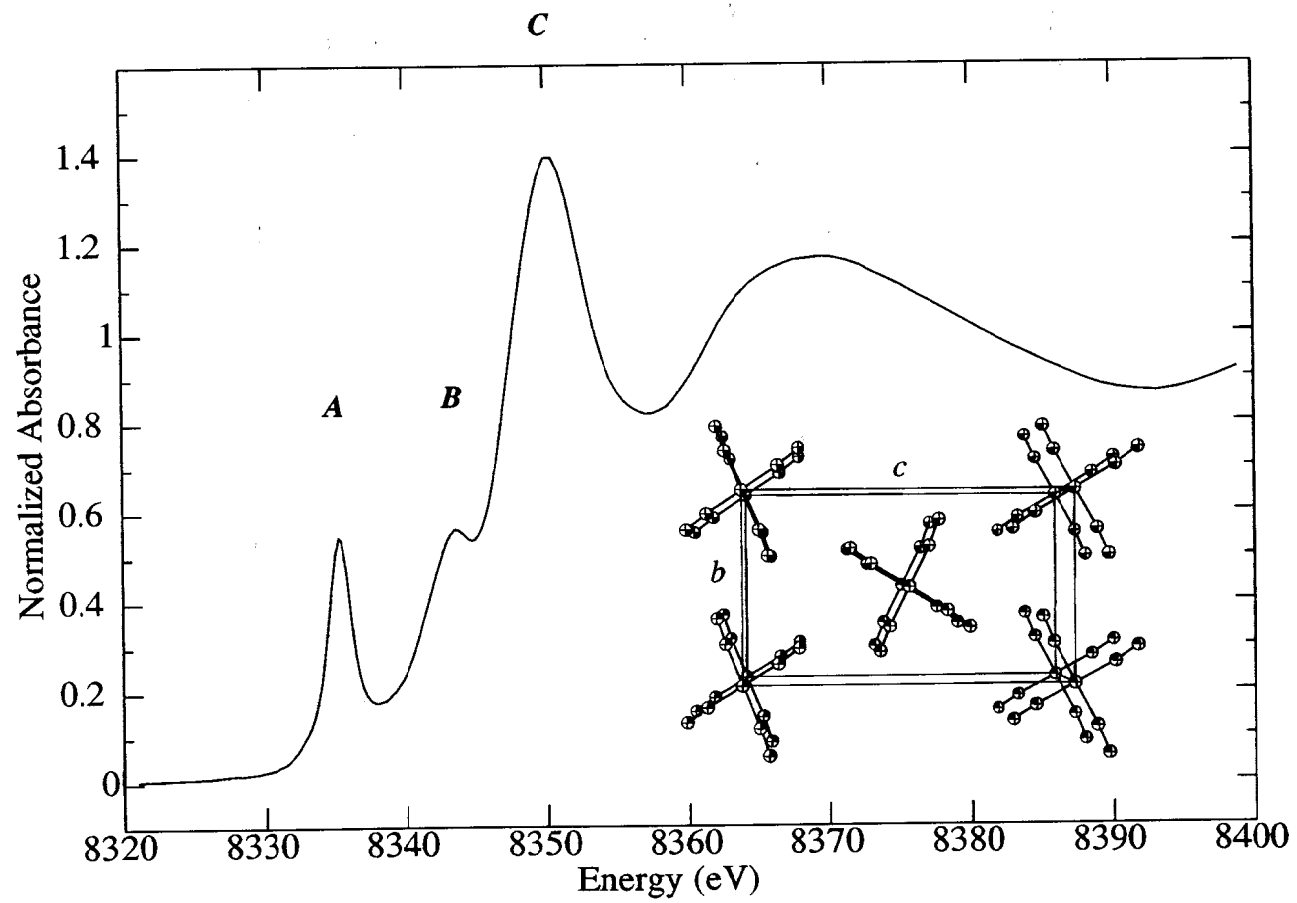
Figure 10

Figure 11

Figure 12

Figure 13